Materials Plus
https://ojs.wiserpub.com/index.php/mp/

Review

Role of Silk in Recent Advances of the Biosensors: A Mini-Review

Orianaisy Gelis Gonzalez, Tianjiao Chen, Xiayan Huang, Ziying Cui, Xueliang Xiao*

Key Laboratory of Eco-textiles, Ministry of Education, Jiangnan University, Wuxi, 214122, China
E-mail: xiao_xueliang@jiangnan.edu.cn

Received: 22 April 2023; **Revised:** 11 December 2023; **Accepted:** 12 December 2023

Abstract: A biosensor is a kind of analytical device that is composed of a biological recognition element associated with a mechanism for stopping and interpreting the signal obtained from the interaction between the analyte and the analytical instrument. More importantly, silk is one of the natural biocompatible substances with incredible strength and flexibility that is widely applied in various applications. Its excellent mechanical properties and versatility have made it an ideal choice for fabricating biosensors, especially electrochemical ones. Therefore, attention to silk-based biosensors increased incredibly over the recent decades, and these biosensors have been deployed as an indispensable research area in the scientific society. Accordingly, this mini-review paper comprehensively investigates the role of silk in the recent advances in biosensors.

***Keywords*:** silk; silk-based biosensor; natural polymer; biocompatibility; electrochemical biosensors

1. Introduction

Biosensors are analytical devices containing an immobilized biological material, such as an enzyme, antibody, nucleic acid, hormone, organelle, or whole-cell, that can interact with an analyte and produce physical, chemical, or electrical signals (Alaejos & García Montelongo, 2004; Alkire et al., 2011; Fan et al., 2020). An analyte is a compound (e.g., glucose, urea, drug, and pesticide); its concentration should be determined by measuring such signals (Hui et al., 2009; Matsumoto et al., 2002; X. Wang et al., 2005). In other words, biosensors are capable of converting their biological actions into measurable signals using the quantitative analysis of various substances (Dzyadevych & Jaffrezic-Renault, 2014; Grieshaber et al., 2008; M. Musameh et al., 2006; Radhakrishnan et al., 2014). The performance of the biosensors is primarily dependent on the stability of the enzyme as well as the specificity and sensitivity of biological reactions. As the great majority of biosensors have immobilized enzymes, silk is an excellent option that can be applied to biosensors. In this regard, silk fibroin proteins offer many chief features which are suitable for enzyme stabilization. Indeed, the structure of silk fibroin proteins has a major role in stabilizing enzymes.

Silk is a natural protein polymer that has been approved as a biocompatible material by the US Food and Drug Administration (FDA) (Padol et al., 2011; Seib & Kaplan, 2013). Silk fibroins generally comprise large internal hydrophobic blocks and relatively large hydrophilic blocks (N- and C-termini) at the chain ends, with small hydrophilic internal blocks (Figure 1). In detail, the sheets containing the polypeptide chains with repeated hydrophobic sequences fold and stack to form hydrophobic crystal blocks (helix structure connecting by backbone hydrogen bonds), whereas the other segments form hydrophilic amorphous domains (H.-J. Jin & Kaplan, 2003; Lu et al., 2010). Moreover, silk is exceptionally known for unrivaled mechanical properties originating from the hierarchical structures from molecular to macroscopic scale (Porter & Vollrath, 2009; Sierra-Montes et al., 2005; Ude et al., 2014). The amino acid sequences aggregate into specific domains with nanosized β-crystalline phase

DOI: https://doi.org/10.37256/2220232897

embedding in an amorphous matrix, where the crystalline domain determines the strength and the amorphous domain decides the toughness.

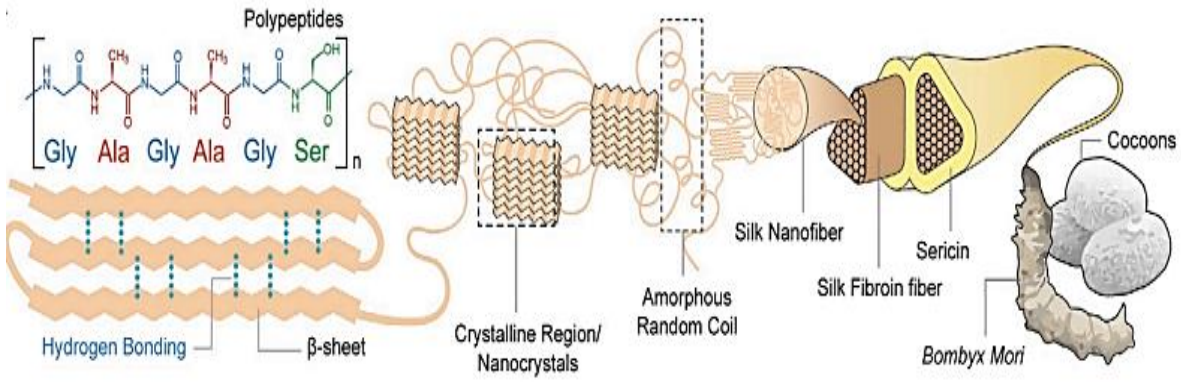

Figure 1. Illustration of the hierarchical structures of silk fiber from B. mori. Adapted with permission from Wiley-VCH (Li et al., 2022)

Spiders, silkworms, and other arthropods are the main source of silk in which the primary component is protein (F. Chen et al., 2012; Fu et al., 2011, 2019). Among the named sources, cocoon silks were derived from silkworms, especially the species of Bombyx mori (B. mori), which have been used worldwide for thousands of years as the most abundant source of silk proteins. In order to extract silk, silkworm cocoons are employed to make silk fibers using factory equipment, mainly being applied in the textile industry (Aigner et al., 2018; Long et al., 2021; Scheller et al., 2001; Teulé et al., 2012; Whittall et al., 2021). In this regard, the regenerated silk fibroin (RSF) extraction method plays a dominant role in building silk-based materials as it is a standard procedure for extracting silk fibers from B. mori cocoons (Rockwood et al., 2011). RSF extraction typically includes degumming, rinsing, dissolution, dialysis, and centrifugation. First, a ternary solvent (combination of CaCl2/ethanol/H2O) or inorganic salts (high concentration LiBr, NaSCN, and ZnCl2 solutions) are used to dissolve degummed silk fibers by breaking hydrogen bonds and disassembling the β-crystalline structures. Then, an aqueous solution of pure RSF will be obtained after completely removing the ions and impurities, which can be lyophilized for long-term storage. Other forms of silk-based materials can also be prepared by dissolving lyophilized RSF in an organic solvent (HFIP: 1,1,1,3,3,3-hexafluoro-2-propanol) (Spiess et al., 2010). In fact, the highly concentrated solutions containing silk protein can be employed for forming critical morphologies such as fibers (Ha et al., 2005), foam (Kluge et al., 2008; Salehi et al., 2020), film (Akon Higuchi, Makoto Yoshida, Takeshi Ohno, 2000; X. Wang et al., 2005), hydrogel (X. Chen et al., 1997; Guziewicz et al., 2011; Kim et al., 2004; Z.-L. Wang et al., 2020), 3-D porous scaffolds (Harris et al., 1998; Tsukada et al., 1994), electro spun, sphere (Humenik et al., 2011; Kucharczyk et al., 2018), and capsules (Hardy & Scheibel, 2009; Hermanson et al., 2007). To provide a relatively high concentration of RSF ionic liquid solution, some organic salts like AminCl and BminCl can dissolve silk fibroins. However, the RSF solutions can solely be exposed to abundant reactive sites for further chemical and functional modifications because silk contains a considerable percentage of amino acids with side chains (such as serine, threonine, aspartic, glutamic, and tyrosine (Murphy & Kaplan, 2009). It should be noted that the degumming treatment and dissolution process inevitably impair the mechanical properties of post-prepared RSF materials due to the breakage of silk fibroin peptide chains and macromolecular degradation (Ho et al., 2012; Y. Jin et al., 2015). The damage to silk fibers can be reduced using a non-alkali solution (urea) instead of an alkali solution (sodium carbonate) for degumming (Yang et al., 2020). Nevertheless, it is feasible to regulate the mechanical features of RSF materials by tuning their conformational transition to β-crystalline structures because the dissolved RSF is present as random coils and meets the demands in various application scenarios (Gao et al., 2020; Hu et al., 2011).

The present mini-review paper aims to study recent papers on biosensors containing silk as the primary material. In this regard, electrochemical biosensors are predominately considered due to the great functionality of silk in such biosensors and their capability to detect signals with high sensitivity and selectivity (Liang et al., 2014; Pal et al., 2016; RICHARD M. WHITE,FELLOW, 1987). The operating principles of electrochemical biosensors mainly rely on the electrochemical properties of the analyte and transducer (Hong et al., 2013). In these kinds of biosensors, an electrochemical reaction occurs on the transducer surface between the bioreceptor and analyte, producing detectable electrochemical signals in terms of voltage, current, impedance, and capacitance (Chaubey & Malhotra, 2002; Malhotra & Ali, 2018; Pisoschi, 2016). Therefore, the role of silk on the performance of the electrochemical biosensors is studied to provide study for readers.

2. Application of Silk-based Materials in Electrochemical Biosensors

As it is clear, silk is a natural polymer that offers high biocompatibility and biodegradability. These two crucial properties are auspicious in that they can encourage scientists to apply them in various applications, especially sensors. Accordingly, Molinnus et al. (Molinnus et al., 2021) fabricated a the biosensor containing a bio-based substrate derived from silk fibroin and combined it with the immobilized enzyme glucose oxidase (GOX). By employing thin- and thick-film technologies, Pt working and counter electrode (upper side), as well as silver/silver chloride (Ag/AgCl) quasi-reference electrode (a conventional standard reference electrode; bottom side), have been prepared, respectively. Four platinum electrodes, two of them as counter electrodes and the others as working electrodes for the aerometric measurements, were applied to each sensor chip.

The glucose sensitivity of the prepared biocompatible glucose biosensor chip was studied in phosphate buffer saline solution (PBS; pH= 7.4), corresponding to the pH value in human blood. The biosensor responded instantaneously with distinct steps to varying glucose concentrations from 0.5 mM to 3 mM with a response time (T90) of about 1 min. As expected, with increasing glucose concentration, the generated current is increasing due to the oxidation of H_2O_2. The corresponding calibration curve is linear in the measured concentration range with a sensitivity of 0.2 ± 0.01 μA/ mM. The experiment was repeated three times. A mean glucose sensitivity of 0.24 ± 0.006 μA/ mM could be achieved in the investigated concentration range measured by three individually prepared biosensors. Since the fibroin substrate is biodegradable only in the presence of proteolytic enzymes, the long-term stability of the fabricated glucose biosensor was proven for more than 100 days in an enzyme-free but moist environment. Between the measurements, the biosensor was stored at 4 ◦C. Different glucose concentrations between 0.5 mM and 3 mM were examined each day. The mean values of three individually fabricated biosensors obtained sensitivities shown as error bars with the corresponding standard deviation. Within the first two days, the sensitivities of the sensors were stable between 0.20 μA/mM and 0.25 μA/ mM, respectively. The average glucose sensitivity decreases within increasing measurement time, and after 100 days, it declines to a value of about 0.05 μA/mM. Several reasons might be responsible for this loss in sensitivity: i) the enzyme can be leached out of the membrane, ii) there is an activity loss of the enzyme, or iii) parts of the enzymatic membrane might be detached from the Pt working electrode.

Apart from its ability to reliably detect glucose levels, a biocompatible and flexible glucose biosensor should also possess long-term stability to withstand the rigors of daily users. Strain onto the flexible substrate with integrated electrodes can be caused by mechanical deformations, which can lead to adverse effects on the sensor performance. Therefore, the platinum electrode's mechanical stability and related degradation have been investigated by repeatedly bending the substrate material for 180◦ by hand. The resistivity change has been recorded by a conventional multimeter after 20, 40, 60, etc., up to 160 cycles. The resistance of the platinum working electrode is increasing from originally ~80 Ω to~115 Ω (N = 3 investigated sensors). Reasons for that might be small crack formations in the Pt layer. On the other hand, despite this resistance increase, the Pt working electrodes still work after 160 bending cycles with 180◦, demonstrating that they can withstand repeated bending without losing functionality.

In this article, silk fibroin is a fundamental polymer in the solution with the platinum electron and silicon resin. However, we consider that this solution can be changed for other natural polymers that have good compatibility with silk fibroin. Indeed, there might have been a mechanical degradation by these synthetic reagents when the mentioned solution was mixed. Therefore, it could be replaced by natural polymers for better performance and compatibility of the biosensor. Figure 2 shows the schematic of the fabrication process for the glucose biosensor.

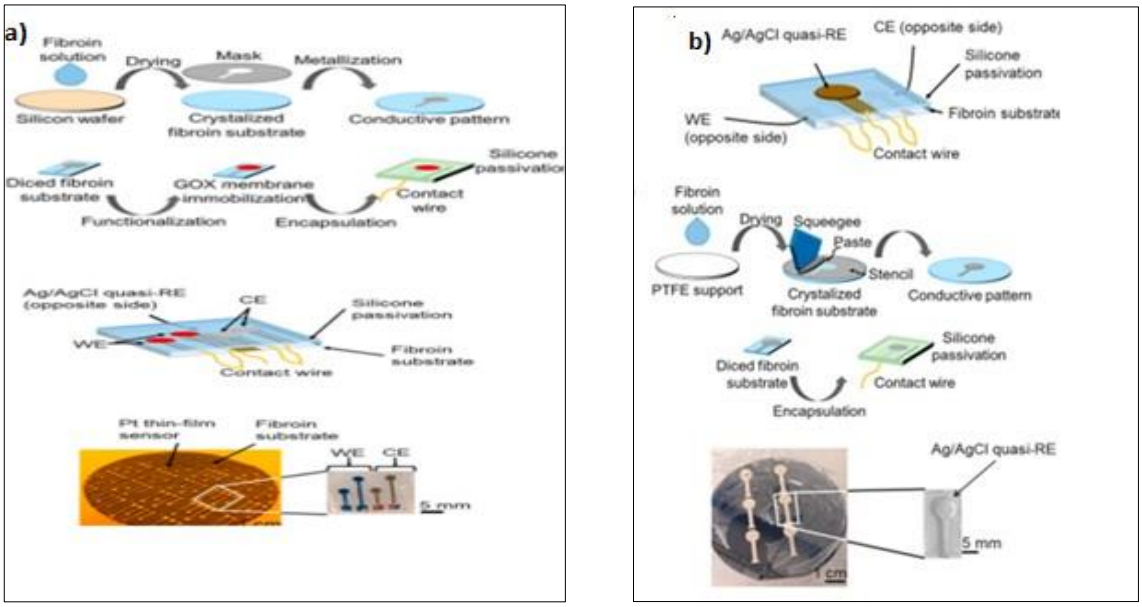

Figure 2. a Fabricated biocompatible glucose biosensor chip via thin- and thick-film technologies with Pt working- and counter electrodes on the upper side and Ag/AgCl quasi-reference electrode at the bottom; (schematically) and light microscopic image of a 4-inch fibroin substrate with thin-film platinum electrodes (left) and diced chip carrying the final Pt working- and counter electrodes (right) b) Fabrication steps of the Ag/AgCl quasi-reference electrode by means of thick-film technology (schematically) and (microscopic photo of 4-inch fibroin substrate with Ag/AgCl quasi-reference electrodes (left) and photo of the final Ag/AgCl quasi-reference electrode (right); GOX: glucose oxidase, RE: reference electrode, WE: working electrode, CE: counter electrode Adapted with permission from Elsevier (Molinnus et al., 2021)

In another form of using silk in biosensors, the enzymatic crosslinked silk fibroin (SF) hydrogel is encapsulated on graphene for the purpose of effect transistor (GFET) by wang et al. (Z. Wang et al., 2021). The SF hydrogel could stabilize the structure of enzymes such as glucose oxidase, which is easy to lose activity. As the SF hydrogel offers low relative permittivity and a stable biological interface, the SF hydrogel encapsulated GFET could detect glucose in solutions with high ionic concentration and a complex mixture of biological components. In addition, the SF hydrogel could be removed easily instead of destroying the properties of grapheme, which enables the excellent renewability of GFET. The sensing mechanism is based on glucose oxidase catalyzing glucose oxidation to produce gluconic acid and H_2O_2. These products lead to a variation in the electric potential of the conducting channel, which could be recorded as signal changes.

In tests, a constant V_{ds} (applied voltage on the channel; 0.1 V) and a swept V_{gs} (actual voltage on the graphene) at a step of 0.02 V were applied to this biosensor. To compare the detection stability between the bare GFET and the SF hydrogel encapsulated GFET in a phosphate buffer saline (PBS) solution system, the PBS solutions with different ionic concentrations (0.01 × PBS ~ 1.62 mM, 0.1 × PBS ~ 16.27 mM, 1 × PBS ~ 162.7 mM) are introduced into the sensing channel **(Figure 3 (a).** The conductance of bare GFET is influenced by the change in ionic concentrations, and the Dirac point had a slight positive shift with the increase of the concentrations of PBS solutions. These results could be interpreted based on the change of double-layer capacitance. This is because C_{dl} is directly related to the ionic concentration (according to the equation: $C_{dl} = \sqrt{2F^2I\varepsilon_0\varepsilon_r}/RT$; where ε_0, ε_r, F, I, R, and T are permittivity of free space, the dielectric constant of the electrolyte, Faraday constant, ionic strength, gas constant, and temperature, respectively). Also, C_{dl} would be increased with the addition of the ionic concentration. However, compared with the bare graphene, it is noticed that the transfer curves of the SF hydrogel encapsulated GFET are unchanged. This is because the SF films formed on the interface reduced the effects of mobile ions on graphene. Consequently, the SF hydrogel encapsulation strategy could be regarded as an effective way to improve the detection stability of GFET in the PBS solution system. The capability of the GFET for glucose detection is tested in a 1 × PBS solution system. V_{Dirac} is the charge neutrality point in the transfer characteristics curve, and it also reflects the Fermi level (EF) of the graphene. The change of the surface potential of graphene ($\Delta\Psi$) has a relationship with ΔEF, which can be expressed as $\Delta EF = q\Delta\Psi$. Thus, the change of surface potential would influence the Dirac point. The regular variations of the Dirac point while sequentially switching various concentrations of glucose solutions demonstrate the concentration-dependent detection. As glucose concentration increases from 1μM to 10mM, V_{Dirac} decreases by 0.08V from 0.44V to 0.36V. The negative shift of the Dirac point could be attributed to the decrease of the surface potential induced by the reaction of HRP with H_2O_2. It also found that the normalized $\Delta V_{Dirac}/\Delta V_{Dirac,\,max}$ shows a good linear relationship with ln [glucose] in the range of 1

μM to 10 mM, where the $\Delta V_{Dirac,\ max} = V_{Dirac,\ 10mM} - V_{Dirac,\ 0}$ with $V_{Dirac,\ 10mM}$ is the Dirac point corresponding to the 10 mM glucose . Moreover, the limit of detection (LOD) for glucose using this biosensor is calculated to be about 200 nm., which is fully capable of detecting glucose at low concentrations. In order to investigate the ability of the SF hydrogel encapsulated GFET to deal with the problem of nonspecific adsorption, Dulbecco's modified eagle medium (DMEM) is selected as the test sample, which consists of inorganic salts, amino acids, glucose, etc. Compared with the bare GFET, the SF hydrogel encapsulated GFET (without glucose oxidase) shows higher robustness under this complex solution system. It is observed that under this channel voltage, the bare graphene tends to absorb some negatively-charged molecules, exhibiting a negative shift of the curve. After the bare GFET is encapsulated by SF, results could be ascribed to the fact that SF hydrogel could act as a physical barrier to filter macromolecules, and SF film also has the effect of isolating charged molecules. In addition, this biosensor shows a noticeable response to the glucose in the DMEM after glucose oxidase is added to the hydrogel **(Figure 3 (b-c).** It can be concluded that the SF hydrogel encapsulated GFET possessed the capability to overcome nonspecific adsorption of non-target molecules on the conducting channel. Eventually, it is notable that the signal values have little fluctuation, with a variation of less than 4.9%. These results demonstrated that the biosensor possesses the capacity for consistently detecting glucose after multiple cycles of usage. The pH of the same concentration decreases the fibroin hydrogel of silk with graphene is not encapsulated, and perform several tests to see if the oxidized glucose can be added in low solutions.

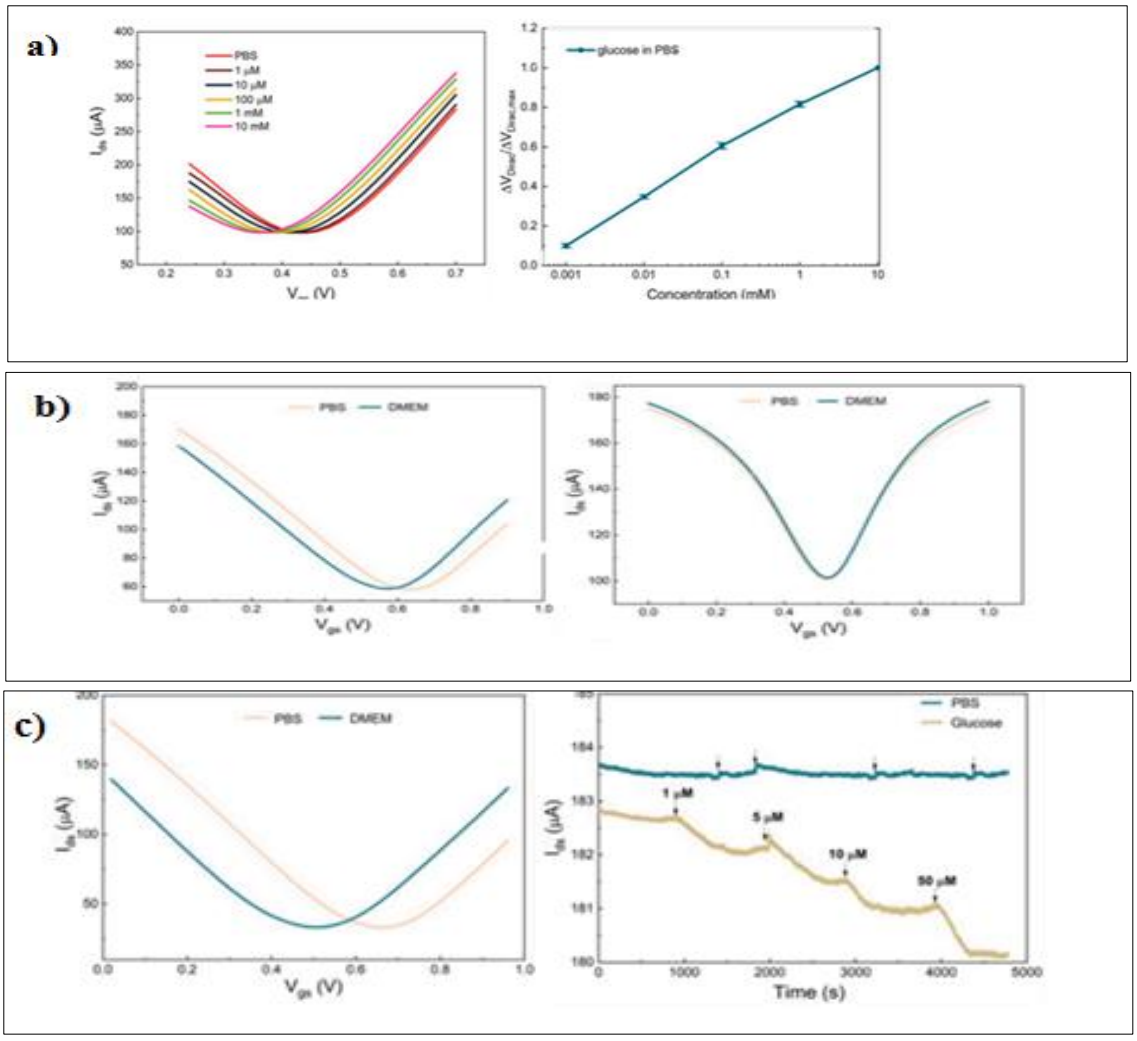

Figure 3. Transfer curves measured (a) when the biosensor was exposed to various glucose concentrations, normalized $\Delta V_{Dirac}/\ \Delta V_{Dirac,\ max}$ as a function of different glucose concentrations, b) bare GFET, SF hydrogel encapsulated GFET (without glucose oxidase), c) SF hydrogel encapsulated GFET (with glucose oxidase), and Channel current responses of the biosensor to the increased glucose concentration in PBS solution measured at VD = 0.1 V and VG = 0.4 V. Adapted with permission from Elsevier (Z. Wang et al., 2021)

Fluorescence lifetime is an essential parameter for understanding fluorescence substances' excited state information. Accordingly, Haroone et al. (Sohail Haroone et al., 2018) have prepared ultrathin films (UTFs) by applying silk as a stabilizer and using the layer-by-layer (LBL) method. The films were composed of 3-

mercaptopropionic acid (3-MPA) functionalized cadmium tellurium quantum dots (CdTe QDs), which were stabilized by silk fibroin (SF) and co-assembled with the double layer of hydroxide (LDH). Firstly, the increase in a fluorescence lifetime from 52.69 ns (QD solution) to 61.71 ns (QD/SF) mixed solution demonstrates the influence of SF on the luminescent properties of CdTe QDs. The fluorescence quantum yield further confirms the luminescence properties of the material. In this regard, the fluorescence quantum yield of the QD aqueous solution and QD/SF mixed solution are 38.92% and 51.63%, respectively. This result highlights the importance of SF in improving the fluorescence property of QDs, which is consistent with the fluorescence intensity variation. All of these observations suggest that SF has stabilized the prepared QDs and prevented the possible aggregation among the QDs. Secondly, the (CdTe QDs@SF/LDH)$_n$ and (CdTe QDs/LDH)$_n$ UTFs was constructed to highlight the role of SF in the UTFs by comparing their fluorescence properties (n= number of layers). The UV absorption value and fluorescence spectra value show an excellent linear relationship with the increase of the number (5-30 layers). Therefore, the presence of silk fibroin in the composition of the ultrathin CdTe quantum dots film can improve luminosity and photoluminescence.

Furthermore, silk fibroin exhibits excellent mechanical properties due to its primary structure of highly repetitive amino acid sequences (GAGAGX) in which the repetitive hexapeptide segments (GAGAGS) can be crystallized, and the rest is believed to contribute to the amorphous place. The SF exists in two conformations (SF-a) and (SF-b), which can be converted into a single conformation by alcohol treatment. The changes of negative elasticity at 195 nm and 217 nm indicate the conformational transformation of SF from random coil to b-sheet. In order to study the effect of different structures of SF on the luminescent properties of CdTe QDs, the two different secondary structures of SF were used to assemble and observe the fluorescence properties of the UTFs ((CdTe QDs/LDH)$_n$, (CdTe QDs@SF-RC/ LDH)$_n$ and (CdTe QDs@SF-b/LDH)$_n$ UTFs). Results indicated the successful assembly and regular growth of CdTe QDs and SF with LDH nanosheets on the quartz substrate during the assembly process. Additionally, the structure of SF-b has a more significant impact on the CdTe QDs, and can be used in the UTFs to detect immunoglobulin (one of the human plasma proteins).

To detect nitric oxide (NO) at nanomolar levels, Musameh et al. (M. M. Musameh et al., 2018) have applied heme-silk films in the presence and absence of oxygen. For this purpose, a silk solution was drop-casted on glassy carbon (GC) electrode, modified with multiwalled carbon nanotubes (MWCNT), and followed by infusion with heme. To optimize the reduction of NO, the performance of the sensor was first evaluated under different pH conditions. To simplify the voltammetric response, the solutions were purged with nitrogen to eliminate oxygen reduction peaks. In the absence of NO, the peak potential of the heme redox couple was shifted to more positive values as the pH decreased. An excellent linear fit was obtained upon plotting heme oxidation or reduction potential versus pH with a slope of 35 mV/pH unit in the case of heme oxidation as protonation is linked to the electrode redox process. In the presence of NO, the NO reduction potential was observed to shift to more positive values with decreasing pH, following a similar trend to the heme redox couple potentials. In addition, the NO reduction current increased as the pH was lowered when a maximum reduction current was observed. The increase in NO reduction current at lower pH is consistent with the more favorable environment for hydroxylamine formation and stabilization at these higher proton concentrations. Moreover, the effect of dissolved oxygen on the heme-silk sensor was tested (Figure 4 (a-d)). In the presence of oxygen, the sensor gave a linear response from 19 nM to 190 nM with a regression (R2) of 0.997, a sensitivity of 145 nA/nM. The presence of oxygen was found not to affect the limit of detection for NO, which was determined to be 2 nm. The slight decrease in sensitivity in the presence of oxygen is due to the partial loss of NO through reaction with oxygen. The ability to operate the sensor in the presence of oxygen is facilitated by a combination of the sensor's well-resolved NO and oxygen reduction peaks and the slower reaction of NO with oxygen at pH 3 compared to that at higher pHs. In addition to oxygen, the effect of other common contaminants was tested. No interference of NO detection by the heme-silk/MWCNT/GC electrode was observed from concentrations of 2 μM dopamine or acetaminophen. Slight interference was observed from 2 μM nitrite and nitrate, corresponding to the response obtained for 19 nM NO. Interference from other common interferences such as ascorbic and uric acid are eliminated as they cannot undergo reduction reactions under the current measurement conditions. Furthermore, it was possible to operate the sensor in the presence of up to 10% calf serum (FBS) without affecting its performance. In many heme-based NO sensors, selectivity is achieved through the use of a perm-selective membrane. However, the results indicated that placing the heme within a silk film's protein environment has improved the sensors' selectivity without requiring the use of a perm-selective membrane. Finally, the operational and storage stability of the sensor was evaluated. The sensor was tested every three to five days, and, when not in use, the electrode was stored at room temperature under dry conditions. The sensor retained 86% of its initial response after two months of this test/storage cycle at room temperature. This stability is significantly better than other heme-based NO sensors recently reported in the literature; in many cases, stability is not reported, or the sensor needs to be stored at 4°C.

In this manuscript, we may observe further harness the benefict of silk in biosensors that produce pleasing outcomes in a flexible ammonia polypyrrole silk/ fiber sensor with assisted by silica nanosphere template for a successful by (She et al., 2021) as shown in Figure 5. The preparation process in this typical experiment,0.62195 g FeCl3·6H2O and 25 mL deionized water were addedinto a beaker to form the FeCl3aqueous solution. Then, a 0.1915mL Py monomer solution was added into 25 mL deionized water.Afterward, both SiO2NS (6%) and Std (5%) were added into thePy aqueous solution. Among them, the SiO2NS template was syn-thesized by the method in Ref.All the solutions were treated ultrasonically until the solutes were dissolved completely.For the growth of PPy, the FeCl3aqueous solution was addeddropwise into the Py solution. Subsequently, the mixture solutionwas solutionwas filled into the glass tube with silk fibers. Then, the glass tube was kept at 4◦C for 15 h. Afterward, we took it out from the solutionand washed with deionized water. The sample was soaked in a ∼10wt% HF solution for 10 min, and then rinsed with deionized water.Finally, the PPy coating silk fibers were dried at 40◦C for 6 h.A similar approach was used for growing sponge-based PPysamples. The sponge sample (about 1.70 cm in length and 0.45 cmin diameter) was cleaned with deionized water without any specialtreatment. Different PPy samples were prepared based on the samesynthesis process and identified as PPy@silk fibers, PPy/NS@silk-fiber, PPy@sponge, and PPy/NS@sponge, respectively.

The as-prepared PPy, PPy@silkfibers, PPy/NS@silk-fiber, PPy@sponge, and PPy/NS@sponge indicates the XRD pattern of PPy, wherein broad peak is around2 _ = 15−30◦originating from the scattering of the PPy chain atthe spacing between crystal surfaces. Whereas, both thePPy@silk fibers and PPy/NS@silk-fiber demonstrate a narrow peakat 20.8◦, mainly due to the silk fiber _ crystal structure . It is worth noting that in the PPy/NS@silk-fiber sample, the diffraction peak at 20.8◦is narrower than that of PPy@silk fibersand closes to the PPy diffraction peak. It shows that the templatecan make the PPy structure more orderly and the Bragg reflection. is relatively clear.No obvious characteristic peak is observedin the PPy@sponge with/without SiO2NS , mainly because the sponge is not in favor of forming an ordered structure.

By creating a gas sensor on flexible silk fibers, the gas-sensing characteristics of the fabricated sensors are examined and contrasted with those of the sponge substrate. The real-time resistance variations of the PPy/NS@silkfiber and PPy/NS@sponge sensors at various NH3 concentrations are captured in Figs. S3 and S4, respectively. Surprisingly, the base resistance of the PPy/NS@silk-fiber sensor is lower, showing that the silk fiber structure is advantageous for the improvement of electrical conductivity. The dynamic response-recovery curves of the PPy/NS@silk-fiber and PPy/NS@sponge sensors exposed to different NH3 concentrations at room temperature are shown in **Fig. 5a**.

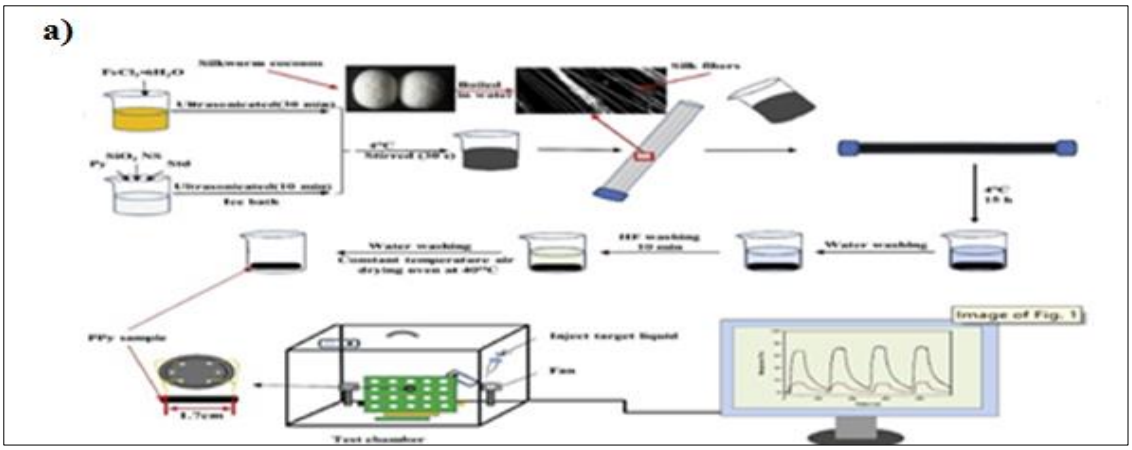

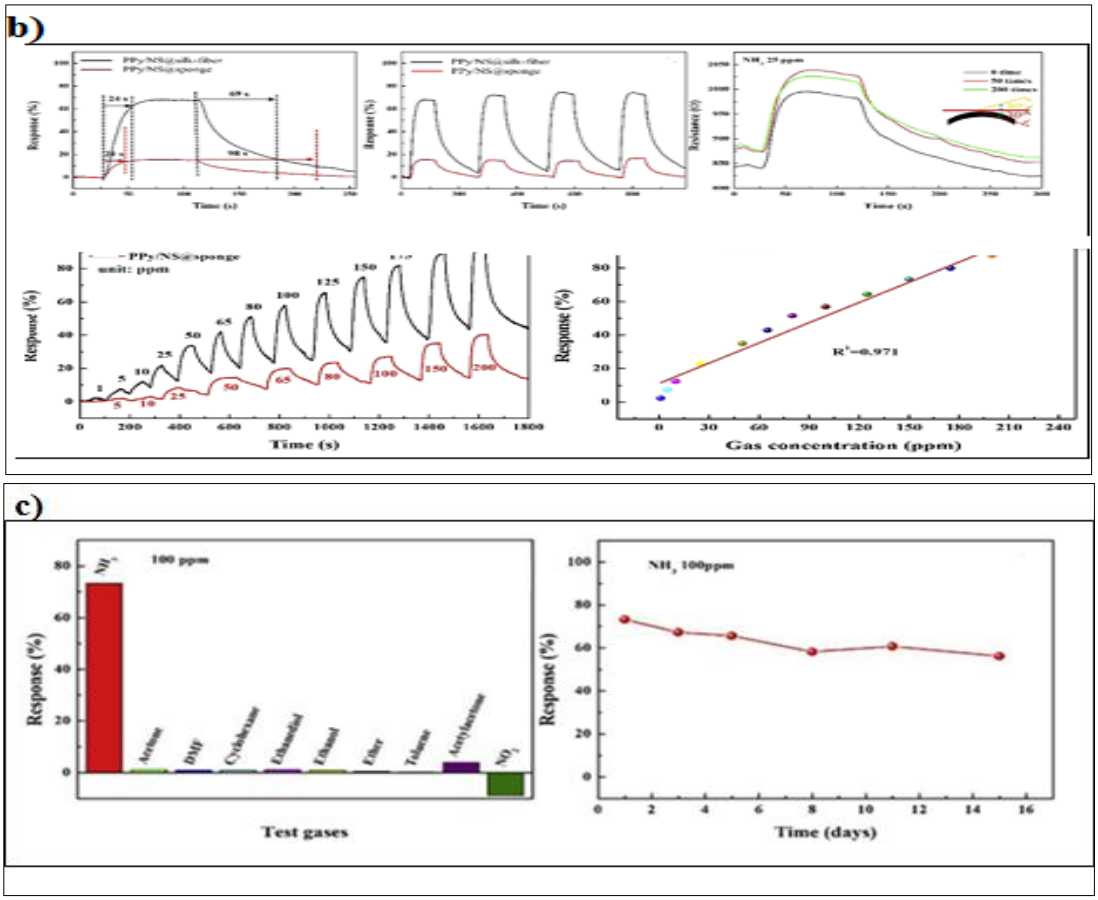

Figure 4. a) illustration of Preparation process schematic of PPy samples. Schematic representation for the gas-sensing performance measurement. Among them, the target liquid is injected through a syringe, and the fans can spread the gas quickly b) illustration the sensing performance of the sensor for NH_3 with different concentrations Dinamic response recovery curves ,Repetibilidad of the Ppy/NS silk fiber sensor for 100 ppm at room and ,Real time resistance changes of the Ppy/NS silk fiber sensor toward 25 ppm NH_3 after 0, 0 and 200 bending cycles alt 30 at room temperature) c)Selectivity of the PPy/NS@silk-fiber sensor towards different test gases at the same concentration (100 ppm), and Long-term stability of the NH3-sensingperformance within the test time of 14 days. . Adapted with permission from Elsevier (She et al., 2021)

The responsiveness of the two sensors gradually increases as the NH3 concentration rises. Notably, the response of the PPy/NS@silk-fiber sensor to 1225 ppmNH3 at ambient temperature is 2-5 times that of the PPy/NS@sponge sensor **(See Fig. 5 a).** The combination of silk fibers and SiO2 NS may boost the sensitivity of sensors to NH3, since the PPy/NS@sponge sensor only reacts to NH3 when the concentration is not less than 5 ppm **(See Fig. 5a**). The sensitization of PPy adsorbent silk fibers should be the source of the outstanding sensing performance (massive response, etc.) of the NS@silk fibers sensor **(Figure 5a)** illustrates how the sensor's reaction depends on the amount of NH3 present and corresponds to the PPy/NS@silk-fiber sensor **(See Fig. 5a).** The sensor's response and NH3 concentration have a linear relationship. With an R2 value of 0.971, the predicted slope is 0.401. The PPy/NS@silk-fiber sensor is a viable choice for real-time NH3 monitoring given that human detection values for NH3 gases are above 5 ppm and the advised exposure limit is 25 ppm . Figure 6a details the dynamic response-recovery curves of the PPy/NS@silk-fiber sensor and a PPy/NS@sponge sensor following exposure to 100 ppm NH3 in order to measure the NH3 sensing response and demonstrate the usefulness of the silk fibers. The NH3 response in the PPy/NS@silk-fiber sensor is estimated to be 73.25 %, which is five times greater. Every gas in-out cycle has nearly identical dynamic properties, which demonstrates the sensor's satisfactory repeatability. In contrast, the PPy/NS@sponge sensor's response value is just a quarter of the PPy/NS@silk-fiber sensor's (See Fig. 5b). Even after the four response-recovery cycles, there is no discernible resistance change, indicating good repeatability of the sensors in their as-developed state. Similarly, **Fig. 5b** depicts the PPy/NS@silk-fiber sensor's flexibility at a 30° bending angle (two-way). After 50 cycles of bending and stretching, the PPy/NS@silk-fiber sensor exhibits only a small (by 4.04 percent) increase in base resistance and little change in response. Even after 200 bending/extension cycles, the response time rarely changes and the response rate drops by 10.61 %. These findings show that the mechanical stability of the PPy/NS@silk-fiber sensor is adequate.

The PPy/NS@silk-fiber sensor works much better than the NH3 sensors that have been described, indicating a potential use for NH3 detection, with a reasonably low detection concentration (LDC) and short response time. An efficient gas sensor must be able to recognize a particular gas only when it is present. In order to explore the gas selectivity, the gas responses of the PPy/NS@silk-fiber sensor to a variety of common volatile organic vapors, including NH3, acetone, N, N-Dimethylformamide (DMF), cyclohexane, ethanediol, ethanol, ether, toluene, and NO2, are compared (See Fig. 5a). The PPy/NS@silk-fiber sensor exhibits good selectivity in separating NH3 from the relevant interfering gas and vapors, according to this research. The great level of selectivity is caused by differences in their sensory systems. The primary cause of the NH3 sensing mechanism is the change in resistance caused by the PPy charge transfer process. The sensing mechanism of PPy for volatile organic vapor is also produced by the adsorption of the gas surface and the oxidation reaction of the gas with the adsorbed oxygen species. Another important metric for assessing the dependability of gas sensors is long-term stability**. Fig. 5c** displays the sensor's long-term stability toward 100 ppm NH3 over a period of 14 days at room temperature. Following that, the answer stays stable (76.82 % of the initial response). The drop in stability is acceptable when compared to the published value of 74 % for detecting NH3 at room temperature for the CdS-adorned PANI sensor. The fine layer of PPy bonded to the fiber surface with SiO2 NS like a mountain range with numerous peaks, according to morphological examination. The PPy/NS@silk-fiber sensor also had additional active sites for enhancing sensing response and dynamic performance, and the silk fibers provide stable support for PPy attachment.

The results of the gas sensing showed that the PPy/NS@silk-fiber sensor responded to the NH3 gas more favorably at room temperature than the PPy/NS@sponge sensor. The PPy/NS@silk-fiber sensor, on the other hand, demonstrated a maximum response of 73.25% as well as flexibility, reproducibility, selectivity, long-term stability, a quick response time of 24 seconds, and a quick recovery time of 69 seconds, towards a gas concentration of 100 ppm NH3 at room temperature. The as-fabricated PPy/NS@silk-fiber sensor, based on the observed gas sensing and the flexible properties of silk, has extensive applications in portable, wearable devices in the industrial market and residential regions due to its low development cost and room-temperature functioning.

Nex we will discuss another biosensor or development based on silk fibroin and with very good results is conductive silk fibroin hydrogel with a semi-interpenetrating network with high toughness and fast self-recovery for strain sensors by (P. Huo et al 2022.). Next, we will see how this sensor was growth:

The fabrication processes of the RSF/PDMA hydrogels are shown **in Fig.6 a-b**. The composited RSF/PDMA gels with a semi-IPN network were prepared using a simple one-pot method. Briefly, all reactants including RSF, DMA, NaCl, and APS were added to a reactor to obtain the homogeneous precursor solution under magnetic stirring. Per sulfate radicals like APS can attack the methyl group of DMAA and form methylene radicals (the alkylation of substituted amides) which can initiate graft chains and lead to a soft self-crosslinking structure without extra cross-linkers. The ratio of free water reduced as the PDMA network steadily formed. RSF is separated during the processes, which speeds up crystallization and results in the development of a -sheet structure. The digital translucent milk-white with light yellow can be used to illustrate this supposition. The design of the composited gel was primarily motivated by the excellent compatibility of RSF and PDMA. The macromolecule and the two components also have a lot of dynamic physical interactions.

The RSF/PDMA composite gels that were created after adding the RSF to the PDMA network had good mechanical properties. The RSF/PDMA gels can support a 1.5 kg heavy reactor with ease, as seen **in Fig.6 c**. additionally; the composite gel was able to withstand various deformations caused by straight-line stretching, twisted stretching, and crossing stretching. In addition, the gel was not easy to puncture by a metal stick even under a large deformation and showed slow in apparent notch expansion during stretching. These results indicated that the introduction of the PDMA network has high compatibility with RSF, and the interactions between the two components also can greatly strengthen the gel.

The mechanical characteristics of RSF/PDMA gels were assessed using tensile and tearing properties testing. Tensile stress increased from 24.2 kPa to 101.7 kPa as the RSF content increased from 0 to 6 wt %, as illustrated in **Fig.6 c**. tensile strain reduced from 2429 % to 518 %. The modulus increased from 4.6 kPa to 54.4 kPa. The fracture energy (Wf) varied from 315.9 kJ/m3 to 717.9 kJ/m3. The compressive property of RSF/PDMA was also significantly improved, as shown in Fig. S2. These findings suggested that the composite hydrogels that were produced had improved mechanical characteristics. As can be seen in Figures 11d and S3, the tearing tests were performed to confirm the impact of RSF.

With an increased RSF ranging from 0% to 6%, the RSF/PDMA gel's tearing energy (T) increased from 112.7 J/m2 to 604.8 J/m2. Due to interactions that can prevent fracture growth, the insertion of the RSF can significantly enhance the tearing energy. Overall, the composite gel demonstrated more comprehensive mechanical properties than the PDMA gel and more softness than pure RSF gel when the RSF concentration was maintained at 4 wt percent. Additionally, the Wf (516.7 kJ/m3) and T (407.3 J/m2) of the RSF/PDMA gel were

2.3 times and 3.6 times bigger than those of the PDMA gel, showing that the RSF/PDMA gel was significantly more durable. As a result, the RSF content was maintained at 4 weight percent for creating the composited hydrogels. Here, the performance of the RSF/PDMA gels for sensing was examined in terms of sensitivity, stability, and linearity. According to **Fig.6 the** gel sensor was stretched at various strains, and each strain step displayed the relative resistance.

When the deformation was maintained for 5 s, the resistance also maintained good stability. Additionally, this gel sensor retained good sensitivity and stability even at greater strains when the gel was stretched by 400 percent. The resistance may practically return to its original value after the sensor is unloaded from a strain of 400 percent, demonstrating outstanding repeatability. When the corresponding resistance change at various strains was fitted **(Fig. 6 d),** it was discovered that the sensing linearity was adequate below the strain of 150 percent and that the gauge factor (GF) was a high 1.03.

A higher GF of 1.84 made the change in resistance more noticeable when the strain was higher than 150 percent**.(Figure 6d-)** illustrates the usage of this gel sensor for bending angle detection with bending angles of 90°, 45°, 30°, and 0°. This gel sensor also demonstrated good linearity between the bending angle and resistance change

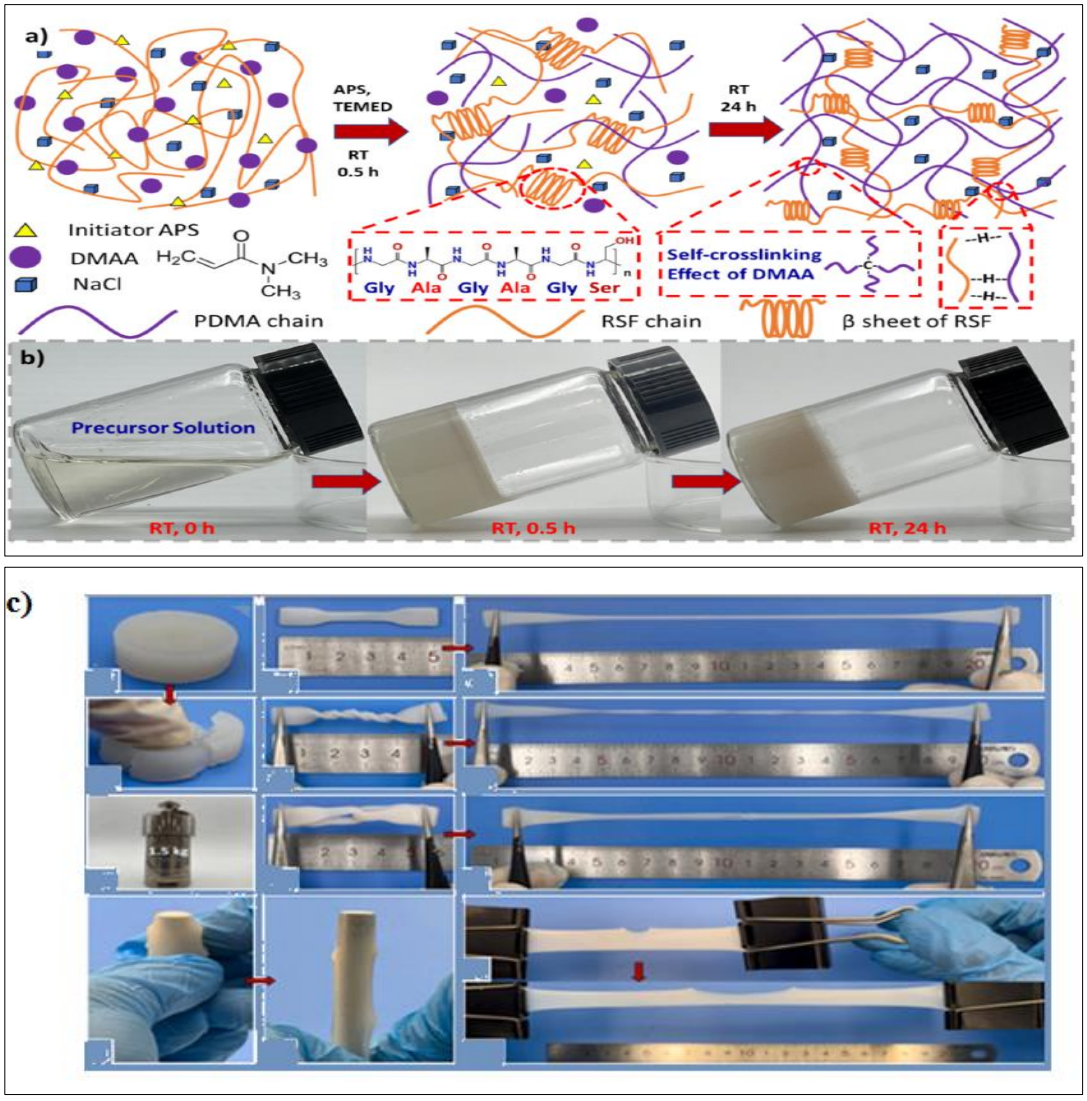

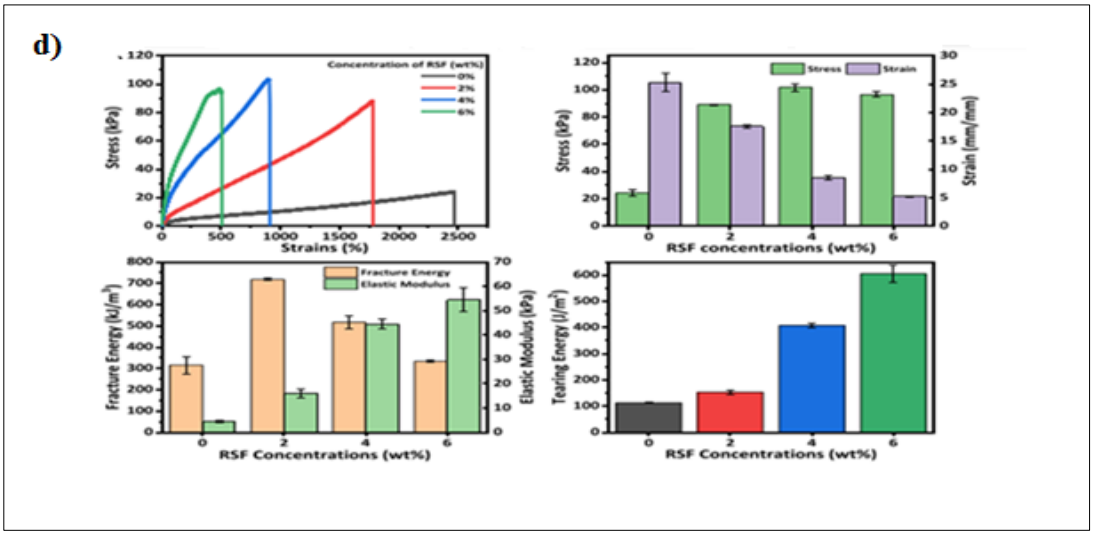

Figure 6. (a) Illustration of the fabrication of the RSF/PDMA composite hydrogels; digital images of the real-time gelatinization processes. b) Illustration of the mechanical properties of RSF gel and RSF/PDMA gels: (a) 5 wt% of RSF gel (Φ25 × H15 mm);the RSF gel was crushed when applied slight compressive force on it; a same size of the RSF/PDMA gel was cut into 3 pieces and it can withstand a 1.5 kg weight; RSF/PDMA gels could resist different deformations: normal stretching; twisted stretching and crossed stretching; gel film covered on a metal stick with large deformation; stretching the notched (~5 mm) gel, c) Mechanical properties of RSF/PDMA gels with different RSF content: tensile stress-strain curves, relevant stress-strain, fracture energy and elastic modulus, tearing energies (T) of PDMA gel and RSF/PDMA gel. Adapted with permission from Elsevier (P. Huo et al 2022.)

Direct attachment of the RSF/PDMA gel sensors to human skin allowed for the detection of numerous body areas and various motion patterns **(Fig.6a-d).** The extreme sensitivity of the gel sensors allow it to detect even the slightest variation in laryngeal movement when a volunteer speaks a variety of syllables. **(Fig.6d).** A maximum strain of 100 percent over 1000 cycles was also used in the cyclic trials, and the sensors showed outstanding stability. Overall, our work is maintained at an above-average level when compared to other comparable resistive type strain sensors, particularly those based on natural materials and ionic conduction, with great sensitivity, admirable linearity, and good stability. The produced gel sensors demonstrated a good potential in flexible wearable, according the aforementioned results.

In this article, applies silk based biosensor with Silk-fibroin film as enzyme stabilizing material and optical signal transducer for developing alcohol oxidase-based µPAD methanol. Hybrid µPAD was designed by using two zones of paper strips (1.4 cm × 1.2 cm) using AKD wax printing as described above**. Scheme 1** (left section) displays the different sections of the hybrid µPAD construct. The top paper strip acted as a sample application zone that helps to remove particles from the samples. The lower paper strip with wave design was used as a spacer between the SF films **(Scheme 1).** The two paper strips were superimposed with the ABTS-SF film in between, while the bi-enzyme SF detection film was placed on the Spacer strip from the rear side. The whole assembly was fixed as a single unit using adhesive tape keeping the Sample zone exposed for dropping the sample (**Steps are shown in Fig.7**). Different concentrations of methanol sample were dropped on the Sample zone and the color developed on the detection film was captured and analyzed. The transparency of SF films was significantly reduced upon immobilization of enzymes in them. The transmittance (%) for the enzyme-free film, AOx immobilized film, and both AOx and HRP (bi-enzyme) immobilized film were 80%, 4% and 1%, respectively **(Fig.7a).** On increasing the immobilized enzyme concentrations, the films developed a whitish texture. This feature is suitable for developing colorimetric sensors due to the high color contrast from the background surface. The average film thickness marginally increased with the immobilization of enzymes as discerned from the FESEM image. The thickness (microns) of the SF film, AOx SF film, and bi-enzyme SF film was 32.6, 35.5, and 37.9, respectively (Fig. S2 b, c, d). The generated SF films were smooth in nature.

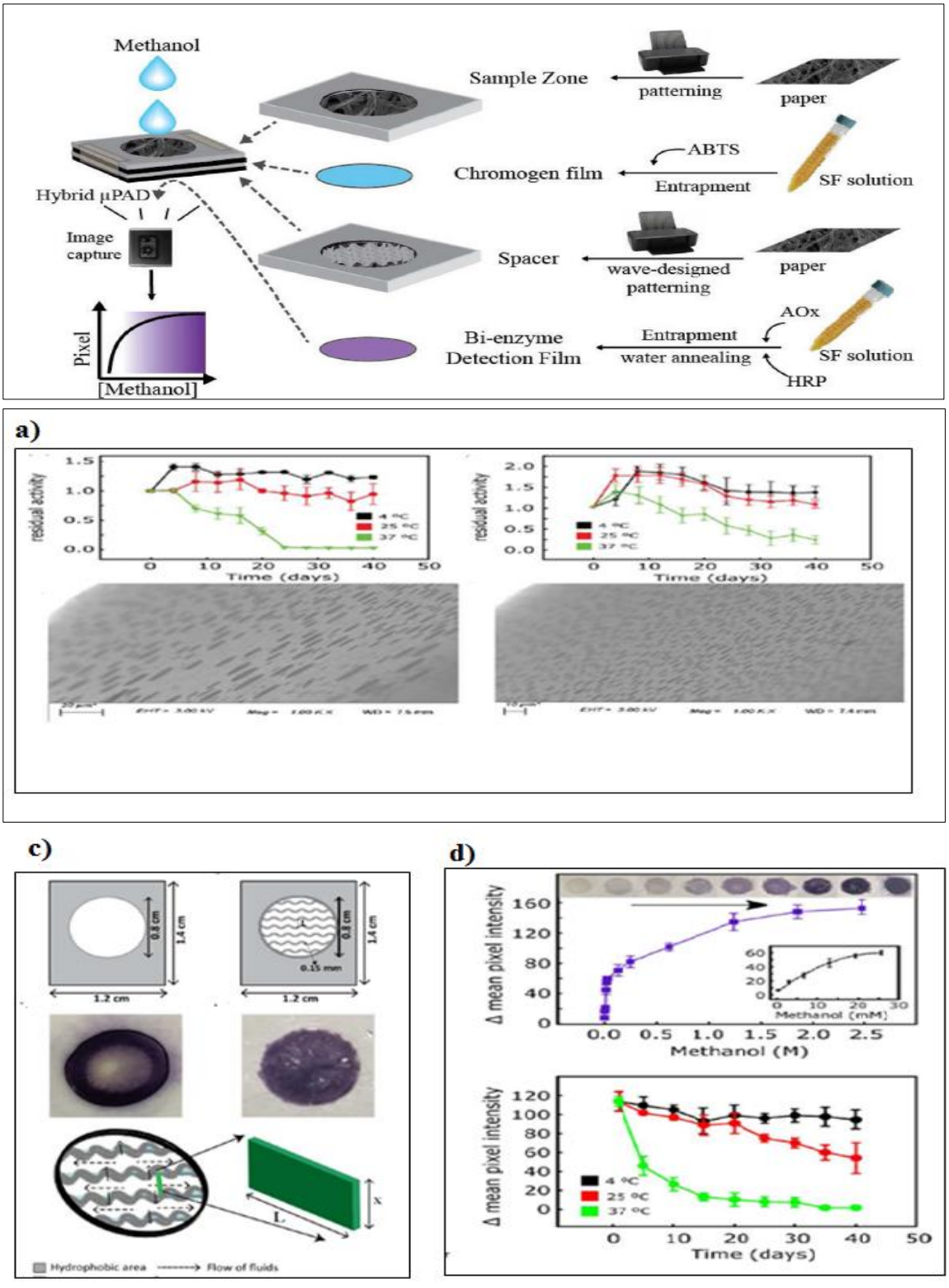

Figure 7. The schematic representation of the different section of the hybrid µPAD and their usage for methanol sensing. (a) Residual activity versus incubation time for dissolvable AOx SF films measured at λ405 nm after 1 min and non-dissolvable AOx SF films measured by mean pixel intensity of the purple color;FESEM images of dissolvable SF film; and non-dissolvable SF film with their corresponding cumulative pore volume versus pore diameter: b) Absorbance spectra of peroxidase reaction system containing AOx-HRP, methanol (25 mM) and with (III) and without (II) SF. Inset: photo of ABTS reaction solution without SF (green) and with SF (purple);Schematic representation of the reaction of different oxidation states of ABTS when it interacts with HRP, H2O2 and then SF. (c) Schematic representation of the reaction of different oxidation states of ABTS when it interacts with HRP, H2O2 and then SF. (For interpretation of the references to color in this figure legend, Scheme of pattern designed for Spacer with circular hydrophilic zone and hydrophilic wave channels within the zone. c)The color developed with 1 M methanol on detection films without wave design pattern on spacer zone;the schematic diagram of the movement of fluid through the channels in the Spacer zone, the response pattern of the µPAD with color changes is shown in the top panel; Stability study of the

μPAD ;the bars indicate standard error (n = 3). (For interpretation of the references to color in this figure legend, the reader. Adapted with permission from Elsevier by (P.D. Thungon et al. 2022)

The activity of the AOx entrapped in dissolvable SF films was analyzed by using HRP-ABTS based assay. Initially, the absorbance at λ405nm increased in the presence of the-substrate, methanol. Interestingly, with increasing reaction time, the solution gradually turned purple instead of the usual green color, which is formed by the ABTS radicals **(Fig. 7a).** A similar result was obtained when H2O2 was used directly in the reaction mixture containing SF instead of the peroxide generating AOx-substrate system. The addition of SF solution to the reaction system (ABTS+ + Methanol + HRP + AOx) lowers the typical peak intensity of ABTS radical at λ405 nm with a concomitant generation of a new peak at ~ λ560 nm **(Fig. 7b)**, turning the final solution to purple **(Fig. 7a inset).** These results demonstrated the key role of SF in transmuting spectral and linked color characteristics in the reaction system. The radical scavenging property of silk fibroin protein may be attributed to the observed fact. The absorbance peak for ABTS at ~ λ570 nm is due to the ABTS dictation or azodication (ABTS2+) formed from the ABTS•+ radical generating the purple color due to the formation of chromogenic –N– – N– azo group and its interaction with the adjacent molecular structures. This rapid peak change along with the formation of a dark purple color has significant advantages for developing sensors because of the sharp color change and the formation of two reciprocally generated peaks (λ405nm vs. λ570nm). Unlike free AOx, the entrapped AOx retained the entire activity for at least up to the 5th day of its preparation at RT Under similar conditions, the free enzyme reduces ~65% of its activity following the incubation period. Interestingly, there was a significant increase in the activity of the immobilized enzyme with the increasing concentration of SF up to the level of 5% (w/v) in the film. The result implies that SF not only stabilizes the enzyme but also facilitates the enzyme- substrate interaction by creating a congenial microenvironment in the soluble state for the diffusion of the substrate. We, however, used 7% (w/ v) SF for preparing the film to facilitate the handling of the delicate film. The optimum concentrations of AOx and HRP in the dissolvable films for maximum activity were identified as 0.5 mg mL 1 for each following one variable at a time approach.

The dissolvable AOx-SF and bi-enzyme SF films were prepared using the optimum concentrations, and the kinetics of the entrapped AOx were examined immediately after setting for 24 h (considered 0 day); the results were compared with free AOx. The dissolvable AOx-SF and bi-enzyme SF films were prepared using the optimum concentrations, and the kinetics of the entrapped AOx were examined immediately after setting for 24 h (considered 0 day); the results were compared with free AOx. The *Km* (mM) of the enzyme in free AOx solution, AOx SF film and bi-enzyme SF films were 1.48 ± 0.2 (20 x 10 ^{3}), 8.41 ± 0.8 (15.2 x 10^{3}), and 2.47 ± 0.1 (18.8 x 10 ^{3}), respectively, with the corresponding rate of reaction (abs min^{1}) as shown in the parentheses. The higher *Km* values and lower reaction rate of the enzyme entrapped in SF films as compared to native AOx may be related to the immobilization effect on the substrate diffusion and interaction with the enzyme binding sites. Both bi-enzyme systems (AOx and HRP) and ABTS were entrapped in SF films separately and later assembled with the paper spacer and detection zones to make an independent μPAD device. The bi-enzyme SF film was rendered to a non-dissolvable form, while the ABTS SF film remained dissolvable. The background color noise in the paper, caused by the aerobic oxidation of ABTS (Fig. S6), could be avoided by entrapping it in the SF film. The entrapped ABTS did not succumb to air oxidation for at least 2 months of storage, contrary to the common phenomena of its increased air oxidation manifested through the formation of green color over (Thungon et al., 2022). The SF film with low oxygen permeability limited the interaction between the entrapped ABTS and atmospheric oxygen, hence halting the oxidation. The dissolvable property of the SF films facilitated quick diffusion of chromogenic from the film to the sample flow through the Spacer strip to the bi-enzyme detection film where the reaction takes place **(Scheme 1).** The optimum concentration of the entrapped ABTS that did not succumb to aerobic oxidation-led-color-change up to 2 months was 10 mM. The stability of the bi-enzyme system in SF film was studied at different temperatures **(Fig. 7b).** Unlike the previous trend **(Fig. 7b and c),** the initial increase pattern of the activity was not observed for the films. The reason may be attributed to the less denaturation of AOx in the bi-enzyme film than that in the mono-enzyme film during the initial preparation time. The activity of the enzyme in non-dissolvable films in terms of Δ means grey pixel intensity was 70 and 90 (with 250 mM methanol) for mono and bi-enzyme film, respectively. The activity of AOx in the bi-enzyme film was thus better than in the mono-enzyme film. The activity retention of bi-enzyme SF films was 90 ± 2% of its initial activity following 40 days of incubation at 4 ◦C.

The analysis could also be viewed through a 2-dimensional shape taking into account the thickness (x) of the paper, in which case area, $A = xL$, where L is the width of the paper zone **(Fig. 7a).** The smaller the value of L, the lower will be the evaporation flux of the fluid over the paper (equation (2) section S1). Hence, segmenting the circular paper zone is likely to reduce the coffee ring effect. Guided by the above principle, we created wave-like designs within the Spacer zone in the μPAD **(Fig. 7 a)** to create more barriers at the edges that will create

turbulence flow of the fluid, slowing the flow and mixing the components in the fluids **(Fig. 7c).** The hydrophobic waves channels, each 0.15 mm thick and separated by hydrophilic space (L mm) between the channels, were created in the zone. When the value of L was reduced, the dye uniformly dispersed over the zone and the pixel intensity increased Hence, the value of L of 1 mm was selected to design the spacer zone for the hybrid μPAD which showed a much better signal on the D film as compared to the design without the wave pattern. The purple color developed on the detection zone could be identified. change as a response signal for methanol, and reduced coffee-ring effect on the detection zone. The shelf life of the highly labile AOx could be markedly improved (57% till 40 days at 25 ◦C) by immobilizing it along with HRP in a non-dissolvable SF-film with pore sizes less than 3.5 μm; this reduced the air diffusion through the film and thus protected the redox enzyme from the inhibitory effect of oxygen. This unprecedented high shelf-life of the AOx enzyme at room temperature will greatly boost its prospect for practical applications. Unlike the typical green color developed during the ABTS-based peroxidase reaction, the intense purple color generated in the SF film facilitated the detection of the signal precisely. Though the dynamic detection range of the developed sensor is exceptionally high, its LoD towards methanol is limited to mM range. Hence, further research is warranted to improve the kinetic parameters of the immobilized enzymes in the SF films. The μPAD biosensor was also sensitive to ethanol (LoD of 0.87 mM). The device has scope for onsite application, following its integration with a suitable smartphone system equipped with a camera having an image processing tool, to capture the colored image developed on the sensor surface for rapid determination of methanol in samples.

3. Conclusions

In this review article, we discuss the great benefit of using silk in the development of electrochemical biosensors in the scientific world. As comprehensively reviewed, the biosensors offer versatile applications in engineering and technology, medicine and biomedical, food safety monitoring, drug delivery, and disease progression. In fact, silk fibroin substrates are efficient in biosensors due to their unique properties such as optical transparency, flexibility, permeability, biocompatibility, and the ability to manage the structure and morphology of regenerated silk fibroin through various processing methods. This material can genuinely have a great potential to be used as the main material to improve the properties of biosensors in detecting target substances. To this end, future works would focus on developing silk-based nanomaterial's and biomolecules on the surface of electrodes or nanoparticles and use new features to fabricate a new generation of biosensors.

Acknowledgments

This work was financially supported by the Opening Project of Key Laboratory of Clean Dyeing and Finishing Technology of Zhejiang Province (Project Number: QIRZ2201), the project from National Advanced Functional Fibre Innovation Centre Co. Ltd. (Grant No. 2022-rw0307), the Opening Project from Jiangsu R&D Center of the Ecological Textile Engineering & Technology of Yancheng Polytechnic College (Grant No. YGKF202207), the project "Trainees from the Universities of Jiangsu Province (P.R. China) sponsored by Qing-Lan Project (Grant No. 1066010241222200)", and the Natural Science Foundation of Jiangsu Province (Grant No. BK20200168).

Conflict of interest

The authors declare no conflict of interest.

References

[1] Aigner, T.B.; DeSimone, E.; Scheibel, T. Biomedical Applications of Recombinant Silk-Based Materials. *Adv. Mater.* **2018**, *30*, e1704636, https://doi.org/10.1002/adma.201704636.
[2] Higuchi, A.; Yoshida, M.; Ohno, T.; Asakura, T.; Hara, M. Production of interferon-β in a culture of fibroblast cells on some polymeric films. *Cytotechnology* **2000**, *34*, 165–173, https://doi.org/10.1023/A:1008130223190.

[3] Alaejos, M.S.; Montelongo, F.J.G. Application of Amperometric Biosensors to the Determination of Vitamins and α-Amino Acids. *Chem. Rev.* **2004**, *104*, 3239–3266, https://doi.org/10.1021/cr0304471.
[4] Alkire, R. C., Kolb, D. M., & Lipkowski, J. (Eds.). (2011). Advances in Electrochemical Science and Engineering (Vol. 13). Wiley. https://doi.org/10.1002/9783527644117
[5] Chaubey, A.; Malhotra, B. Mediated biosensors. *Biosens. Bioelectron.* **2002**, *17*, 441–456, https://doi.org/10.1016/s0956-5663(01)00313-x.
[6] Chen, F.; Porter, D.; Vollrath, F. Morphology and structure of silkworm cocoons. *Mater. Sci. Eng. C* **2012**, *32*, 772–778, https://doi.org/10.1016/j.msec.2012.01.023.
[7] Chen, X., Li, W., Zhong, W., Lu, Y., & Yu, T. (1997). pH sensitivity and ion sensitivity of hydrogels based on complex-forming chitosan/silk fibroin interpenetrating polymer network. Journal of Applied Polymer Science, 65(11), 2257–2262. https://doi.org/10.1002/(SICI)1097-4628(19970912)65:11<2257::AID-APP23>3.0.CO;2-Z
[8] Dzyadevych, S., & Jaffrezic-Renault, N. (2014). Conductometric biosensors. In Biological Identification (pp. 153–193). Elsevier. https://doi.org/10.1533/9780857099167.2.153
[9] Fan, Q.; Li, J.; Zhu, Y.; Yang, Z.; Shen, T.; Guo, Y.; Wang, L.; Mei, T.; Wang, J.; Wang, X. Functional Carbon Quantum Dots for Highly Sensitive Graphene Transistors for Cu^{2+} Ion Detection. *ACS Appl. Mater. Interfaces* **2020**, *12*, 4797–4803, https://doi.org/10.1021/acsami.9b20785.
[10] Fu, C.; Porter, D.; Chen, X.; Vollrath, F.; Shao, Z. Understanding the Mechanical Properties of *Antheraea Pernyi* Silk—From Primary Structure to Condensed Structure of the Protein. *Adv. Funct. Mater.* **2011**, *21*, 729–737, https://doi.org/10.1002/adfm.201001046.
[11] Fu, C.; Wang, Y.; Guan, J.; Chen, X.; Vollrath, F.; Shao, Z. Cryogenic toughness of natural silk and a proposed structure–function relationship. *Mater. Chem. Front.* **2019**, *3*, 2507–2513, https://doi.org/10.1039/c9qm00282k.
[12] Gao, W.; Wang, M.; Bai, H. A review of multifunctional nacre-mimetic materials based on bidirectional freeze casting. *J. Mech. Behav. Biomed. Mater.* **2020**, *109*, 103820, https://doi.org/10.1016/j.jmbbm.2020.103820.
[13] Grieshaber, D.; MacKenzie, R.; Vörös, J.; Reimhult, E. Electrochemical Biosensors - Sensor Principles and Architectures. *Sensors* **2008**, *8*, 1400–1458, https://doi.org/10.3390/s80314000.
[14] Guziewicz, N.; Best, A.; Perez-Ramirez, B.; Kaplan, D.L. Lyophilized silk fibroin hydrogels for the sustained local delivery of therapeutic monoclonal antibodies. *Biomaterials* **2011**, *32*, 2642–2650, https://doi.org/10.1016/j.biomaterials.2010.12.023.
[15] Ha, S.-W.; Tonelli, A.E.; Hudson, S.M. Structural Studies of *Bombyx mori* Silk Fibroin during Regeneration from Solutions and Wet Fiber Spinning. *Biomacromolecules* **2005**, *6*, 1722–1731, https://doi.org/10.1021/bm050010y.
[16] Hardy, J.G.; Scheibel, T.R. Production and processing of spider silk proteins. *J. Polym. Sci. Part A: Polym. Chem.* **2009**, *47*, 3957–3963, https://doi.org/10.1002/pola.23484.
[17] Harris, L. D., Kim, B.-S., & Mooney, D. J. (1998). Open pore biodegradable matrices formed with gas foaming. Journal of Biomedical Materials Research, 42(3), 396–402. https://doi.org/10.1002/(SICI)1097-4636(19981205)42:3<396::AID-JBM7>3.0.CO;2-E
[18] Hermanson, K.D.; Huemmerich, D.; Scheibel, T.; Bausch, A.R. Engineered Microcapsules Fabricated from Reconstituted Spider Silk. *Adv. Mater.* **2007**, *19*, 1810–1815, https://doi.org/10.1002/adma.200602709.
[19] Ho, M.-P.; Wang, H.; Lau, K.-T. Effect of degumming time on silkworm silk fibre for biodegradable polymer composites. *Appl. Surf. Sci.* **2012**, *258*, 3948–3955, https://doi.org/10.1016/j.apsusc.2011.12.068.
[20] Hong, J.; Zhao, Y.-X.; Xiao, B.-L.; Moosavi-Movahedi, A.A.; Ghourchian, H.; Sheibani, N. Direct Electrochemistry of Hemoglobin Immobilized on a Functionalized Multi-Walled Carbon Nanotubes and Gold Nanoparticles Nanocomplex-Modified Glassy Carbon Electrode. *Sensors* **2013**, *13*, 8595–8611, https://doi.org/10.3390/s130708595.
[21] Hu, X.; Shmelev, K.; Sun, L.; Gil, E.-S.; Park, S.-H.; Cebe, P.; Kaplan, D.L. Regulation of Silk Material Structure by Temperature-Controlled Water Vapor Annealing. *Biomacromolecules* **2011**, *12*, 1686–1696, https://doi.org/10.1021/bm200062a.
[22] Hui, N.; Gao, R.-F.; Li, X.-Q.; Sun, W.; Jiao, K. Direct electrochemistry of hemoglobin immobilized in polyvinylalcohol and clay composite film modified carbon ionic liquid electrode. *J. Braz. Chem. Soc.* **2009**, *20*, 252–258, https://doi.org/10.1590/s0103-50532009000200009.
[23] Humenik, M.; Smith, A.M.; Scheibel, T. Recombinant Spider Silks—Biopolymers with Potential for Future Applications. *Polymers* **2011**, *3*, 640–661, https://doi.org/10.3390/polym3010640.
[24] Huo, P.; Ding, H.; Tang, Z.; Liang, X.; Xu, J.; Wang, M.; Liang, R.; Sun, G. Conductive silk fibroin hydrogel with semi-interpenetrating network with high toughness and fast self-recovery for strain sensors. *Int. J. Biol. Macromol.* **2022**, *212*, 1–10, https://doi.org/10.1016/j.ijbiomac.2022.05.084.
[25] Jin, H.-J.; Kaplan, D.L. Mechanism of silk processing in insects and spiders. *Nature* **2003**, *424*, 1057–1061, https://doi.org/10.1038/nature01809.

[26] Jin, Y.; Kundu, B.; Cai, Y.; Kundu, S.C.; Yao, J. Bio-inspired mineralization of hydroxyapatite in 3D silk fibroin hydrogel for bone tissue engineering. *Colloids Surfaces B: Biointerfaces* **2015**, *134*, 339–345, https://doi.org/10.1016/j.colsurfb.2015.07.015.
[27] Kim, U.-J.; Park, J.; Li, C.; Jin, H.-J.; Valluzzi, R.; Kaplan, D.L. Structure and Properties of Silk Hydrogels. *Biomacromolecules* **2004**, *5*, 786–792, https://doi.org/10.1021/bm0345460.
[28] Kluge, J.A.; Rabotyagova, O.; Leisk, G.G.; Kaplan, D.L. Spider silks and their applications. *Trends Biotechnol.* **2008**, *26*, 244–251, https://doi.org/10.1016/j.tibtech.2008.02.006.
[29] Kucharczyk, K.; Weiss, M.; Jastrzebska, K.; Luczak, M.; Ptak, A.; Kozak, M.; Mackiewicz, A.; Dams-Kozlowska, H. Bioengineering the spider silk sequence to modify its affinity for drugs. *Int. J. Nanomed.* **2018**, *ume 13*, 4247–4261, https://doi.org/10.2147/ijn.s168081.
[30] Li, C.; Wu, J.; Shi, H.; Xia, Z.; Sahoo, J.K.; Yeo, J.; Kaplan, D.L. Fiber-Based Biopolymer Processing as a Route toward Sustainability. *Adv. Mater.* **2021**, *34*, 2105196–e2105196, https://doi.org/10.1002/adma.202105196.
[31] Liang, B.; Fang, L.; Hu, Y.; Yang, G.; Zhu, Q.; Ye, X. Fabrication and application of flexible graphene silk composite film electrodes decorated with spiky Pt nanospheres. *Nanoscale* **2014**, *6*, 4264–4274, https://doi.org/10.1039/c3nr06057h.
[32] Long, D.; Cheng, X.; Hao, Z.; Sun, J.; Umuhoza, D.; Liu, Y.; Chen, L.; Xiang, Z.; Yang, F.; Zhao, A. Genetic hybridization of highly active exogenous functional proteins into silk-based materials using "light-clothing" strategy. *Matter* **2021**, *4*, 2039–2058, https://doi.org/10.1016/j.matt.2021.03.020.
[33] Lu, Q.; Hu, X.; Wang, X.; Kluge, J.A.; Lu, S.; Cebe, P.; Kaplan, D.L. Water-insoluble silk films with silk I structure. *Acta Biomater.* **2010**, *6*, 1380–1387, https://doi.org/10.1016/j.actbio.2009.10.041.
[34] Malhotra, B.D.; Ali, A. Nanomaterials in Biosensors: Fundamentals and Applications. In *Nanomaterials for Biosensors*; Elsevier: Amsterdam, The Netherlands, 2018; pp. 1–74; doi:10.1016/b978-0-323-44923-6.00001-7.
[35] Matsumoto, T.; Ohashi, A.; Ito, N. Development of a micro-planar Ag/AgCl quasi-reference electrode with long-term stability for an amperometric glucose sensor. *Anal. Chim. Acta* **2002**, *462*, 253–259, https://doi.org/10.1016/s0003-2670(02)00334-3.
[36] Molinnus, D.; Drinic, A.; Iken, H.; Kröger, N.; Zinser, M.; Smeets, R.; Köpf, M.; Kopp, A.; Schöning, M.J. Towards a flexible electrochemical biosensor fabricated from biocompatible Bombyx mori silk. *Biosens. Bioelectron.* **2021**, *183*, 113204, https://doi.org/10.1016/j.bios.2021.113204.
[37] Murphy, A.R.; Kaplan, D.L. Biomedical applications of chemically-modified silk fibroin. *J. Mater. Chem.* **2009**, *19*, 6443–6450, https://doi.org/10.1039/b905802h.
[38] Musameh, M.M.; Dunn, C.J.; Uddin, H.; Sutherland, T.D.; Rapson, T.D. Silk provides a new avenue for third generation biosensors: Sensitive, selective and stable electrochemical detection of nitric oxide. *Biosens. Bioelectron.* **2018**, *103*, 26–31, https://doi.org/10.1016/j.bios.2017.12.019.
[39] Musameh, M.; Moezzi, N.; Schauman, L.M.; Meyerhoff, M.E. Glutathione Peroxidase-Based Amperometric Biosensor for the Detection of *S*-Nitrosothiols. *Electroanalysis* **2006**, *18*, 2043–2048, https://doi.org/10.1002/elan.200603659.
[40] Padol, A.; Jayakumar, K.; Shridhar, N.; Swamy, N.; Swamy, N.; Mohan, K. Safety evaluation of silk protein film (A novel wound healing agent) in terms of acute dermal toxicity, acute dermal irritation and skin sensitization. *Toxicol. Int.* **2011**, *18*, 17–21, https://doi.org/10.4103/0971-6580.75847.
[41] Pal, R.K.; Farghaly, A.A.; Wang, C.; Collinson, M.M.; Kundu, S.C.; Yadavalli, V.K. Conducting polymer-silk biocomposites for flexible and biodegradable electrochemical sensors. *Biosens. Bioelectron.* **2016**, *81*, 294–302, https://doi.org/10.1016/j.bios.2016.03.010.
[42] Pisoschi, A.M. Potentiometric Biosensors: Concept and Analytical Applications-An Editorial. *Biochem. Anal. Biochem.* **2016**, *5*, https://doi.org/10.4172/2161-1009.1000e164.
[43] Porter, D.; Vollrath, F. Silk as a Biomimetic Ideal for Structural Polymers. *Adv. Mater.* **2009**, *21*, 487–492, https://doi.org/10.1002/adma.200801332.
[44] Radhakrishnan, R.; Suni, I.I.; Bever, C.S.; Hammock, B.D. Impedance Biosensors: Applications to Sustainability and Remaining Technical Challenges. *ACS Sustain. Chem. Eng.* **2014**, *2*, 1649–1655, https://doi.org/10.1021/sc500106y.
[45] RICHARD M. WHITE,FELLOW, I. (1987). A Sensor Classification Scheme. UFFC-34, 124–126.
[46] Rockwood, D.N.; Preda, R.C.; Yücel, T.; Wang, X.; Lovett, M.L.; Kaplan, D.L. Materials fabrication from Bombyx mori silk fibroin. *Nat. Protoc.* **2011**, *6*, 1612–1631, https://doi.org/10.1038/nprot.2011.379.
[47] Salehi, S.; Koeck, K.; Scheibel, T. Spider Silk for Tissue Engineering Applications. *Molecules* **2020**, *25*, 737, doi:10.3390/molecules25030737.
[48] Scheller, J.; Gührs, K.-H.; Grosse, F.; Conrad, U. Production of spider silk proteins in tobacco and potato. *Nat. Biotechnol.* **2001**, *19*, 573–577, https://doi.org/10.1038/89335.
[49] Seib, F.P.; Kaplan, D.L. Silk for Drug Delivery Applications: Opportunities and Challenges. *Isr. J. Chem.* **2013**, *53*, 756–766, https://doi.org/10.1002/ijch.201300083.

[50] She, C.; Li, G.; Zhang, W.; Xie, G.; Zhang, Y.; Li, L.; Yue, F.; Liu, S.; Jing, C.; Cheng, Y.; et al. A flexible polypyrrole/silk-fiber ammonia sensor assisted by silica nanosphere template. *Sensors Actuators A: Phys.* **2020**, *317*, 112436, https://doi.org/10.1016/j.sna.2020.112436.
[51] Sierra-Montes, J.M.; Pereira-Simon, S.; Smail, S.S.; Herrera, R.J. The silk moth Bombyx mori U1 and U2 snRNA variants are differentially expressed. *Gene* **2005**, *352*, 127–136, https://doi.org/10.1016/j.gene.2005.02.013.
[52] Haroone, M.S.; Li, L.; Ahmad, A.; Huang, Y.; Ma, R.; Zhang, P.; Hu, Y.; Kaleem, Q.M.; Lu, J. Luminous composite ultrathin films of CdTe quantum dots/silk fibroin co-assembled with layered doubled hydroxide: Enhanced photoluminescence and biosensor application. *J. Materiomics* **2018**, *4*, 165–171, https://doi.org/10.1016/j.jmat.2018.05.002.
[53] Spiess, K.; Lammel, A.; Scheibel, T. Recombinant Spider Silk Proteins for Applications in Biomaterials. *Macromol. Biosci.* **2010**, *10*, 998–1007, https://doi.org/10.1002/mabi.201000071.
[54] Teulé, F.; Miao, Y.-G.; Sohn, B.-H.; Kim, Y.-S.; Hull, J.J.; Fraser, M.J.; Lewis, R.V.; Jarvis, D.L. Silkworms transformed with chimeric silkworm/spider silk genes spin composite silk fibers with improved mechanical properties. *Proc. Natl. Acad. Sci.* **2012**, *109*, 923–928, https://doi.org/10.1073/pnas.1109420109.
[55] Thungon, P.D.; Kuri, P.R.; Bachu, V.; Goswami, P. Silk-fibroin film as enzyme stabilizing material and optical signal transducer for developing alcohol oxidase-based μPAD methanol biosensor. *Biosens. Bioelectron. X* **2022**, *11*, https://doi.org/10.1016/j.biosx.2022.100147.
[56] Tsukada, M.; Freddi, G.; Minoura, N.; Allara, G. Preparation and application of porous silk fibroin materials. *J. Appl. Polym. Sci.* **1994**, *54*, 507–514, https://doi.org/10.1002/app.1994.070540411.
[57] Ude, A.; Eshkoor, R.; Zulkifili, R.; Ariffin, A.; Dzuraidah, A.; Azhari, C. Bombyx mori silk fibre and its composite: A review of contemporary developments. *Mater. Des.* **2014**, *57*, 298–305, https://doi.org/10.1016/j.matdes.2013.12.052.
[58] Wang, X.; Kim, H.J.; Xu, P.; Matsumoto, A.; Kaplan, D.L. Biomaterial Coatings by Stepwise Deposition of Silk Fibroin. *Langmuir* **2005**, *21*, 11335–11341, https://doi.org/10.1021/la051862m.
[59] Wang, Z.-L.; Shen, Y.-H.; Sun, X.; Li, Z.-H.; Wang, X.-Y.; Zhao, Z. High biocompatible AuNCs-silk fibroin hydrogel system for visual detection of H2O2. *Microchem. J.* **2020**, *157*, 105036, https://doi.org/10.1016/j.microc.2020.105036.
[60] Wang, Z.; Yu, H.; Zhao, Z. Silk fibroin hydrogel encapsulated graphene filed-effect transistors as enzyme-based biosensors. *Microchem. J.* **2021**, *169*, 106585, https://doi.org/10.1016/j.microc.2021.106585.
[61] Whittall, D.R.; Baker, K.V.; Breitling, R.; Takano, E. Host Systems for the Production of Recombinant Spider Silk. *Trends Biotechnol.* **2020**, *39*, 560–573, https://doi.org/10.1016/j.tibtech.2020.09.007.
[62] Yang, H., Wang, Z., Wang, M., & Li, C. (2020). Structure and properties of silk fibroin aerogels prepared by non-alkali degumming process. Polymer, 192, 122298. https://doi.org/10.1016/j.polymer.2020.122298.